

Process development of a SARS-CoV-2 nanoparticle vaccine

Diandra Martinez-Cano^{a,*}, Rashmi Ravichandran^{b,c}, Huong Le^a, H. Edward Wong^a, Bharat Jagannathan^a, Erik J. Liu^a, William Bailey^a, Jane Yang^a, Kelli Matthies^a, Hedieh Barkhordarian^a, Bhavana Shah^a, Nithya Srinivasan^a, Jun Zhang^a, Angel Hsu^a, Jette Wypych^a, Jennitte Stevens^a, Deirdre Murphy Piedmonte^a, Les P. Miranda^a, Lauren Carter^{b,c}, Michael Murphy^{b,c}, Neil P. King^{b,c}, Neil Soice^a

^a Process Development, Amgen Inc., Amgen Center Drive, Thousand Oaks, CA 91320, USA

^b Department of Biochemistry, University of Washington, Seattle, WA 98195, USA

^c Institute for Protein Design, University of Washington, Seattle, WA 98195, USA

ARTICLE INFO

Keywords:

SARS-CoV-2
COVID-19
Nanoparticle vaccine
Process development
First-in-human

ABSTRACT

One of the outcomes from the global COVID-19 pandemic caused by SARS-CoV-2 has been an acceleration of development timelines to provide treatments in a timely manner. For example, it has recently been demonstrated that the development of monoclonal antibody therapeutics from vector construction to IND submission can be achieved in five to six months rather than the traditional ten-to-twelve-month timeline using CHO cells [1,2]. This timeline is predicated on leveraging existing, robust platforms for upstream and downstream processes, analytical methods, and formulation. These platforms also reduce; the requirement for ancillary studies such as cell line stability, or long-term product stability studies. Timeline duration was further reduced by employing a transient cell line for early material supply and using a stable cell pool to manufacture toxicology study materials. The development of non-antibody biologics utilizing traditional biomanufacturing processes in CHO cells within a similar timeline presents additional challenges, such as the lack of platform processes and additional analytical assay development. In this manuscript, we describe the rapid development of a robust and reproducible process for a two-component self-assembling protein nanoparticle vaccine for SARS-CoV-2. Our work has demonstrated a successful academia-industry partnership model that responded to the COVID-19 global pandemic quickly and efficiently and could improve our preparedness for future pandemic threats.

1. Introduction

In response to the COVID-19 (Coronavirus disease 2019) pandemic, the King and Veesler labs and the Institute for Protein Design (IPD) at the University of Washington developed a self-assembling protein nanoparticle vaccine candidate displaying 60 copies of the receptor-binding domain (RBD) of the SARS-CoV-2 (severe acute respiratory syndrome coronavirus 2) spike protein in a highly immunogenic array [3]. The nanoparticle immunogen has been shown to elicit potent neutralizing antibody responses against SARS-CoV-2 in mice [3] and humans [4], and a related vaccine based on the same nanoparticle immunogen recently met its co-primary endpoints in a Phase 3 clinical trial. The nanoparticle immunogen is based on the computationally designed two-component nanoparticle 153–50 [5] and comprises multiple copies of two distinct protein subunits. Component A, which bears the RBD as a

genetic fusion to its N terminus, is trimeric and derived from an aldolase of the hyperthermophilic bacterium *T. maritima* [6]. Component B, which interacts with Component A via a computationally designed interface to drive nanoparticle assembly, is a pentameric subunit derived from a bacterial lumazine synthase [7]. When mixed in an equimolar ratio, these components spontaneously assemble to form a 120-subunit nanoparticle consisting of 12 pentamers and 20 trimers, arranged with icosahedral point group symmetry [8]. Several nanoparticle immunogens based on computationally designed two-component nanoparticles have been evaluated preclinically over the last few years. Among them, three nanoparticles for respiratory syncytial virus (RSV) [9], influenza [10], and SARS-CoV-2 [8] entered clinical trials in 2021. Given the exigencies of the COVID-19 pandemic, in 2020, the IPD and Amgen formed a partnership to combine existing knowledge on the two-component nanoparticle platform with extensive process development experience

* Corresponding author.

E-mail address: dmarti07@amgen.com (D. Martinez-Cano).

<https://doi.org/10.1016/j.procbio.2023.03.014>

Received 8 August 2022; Received in revised form 18 February 2023; Accepted 12 March 2023

Available online 17 March 2023

1359-5113/© 2023 Published by Elsevier Ltd.

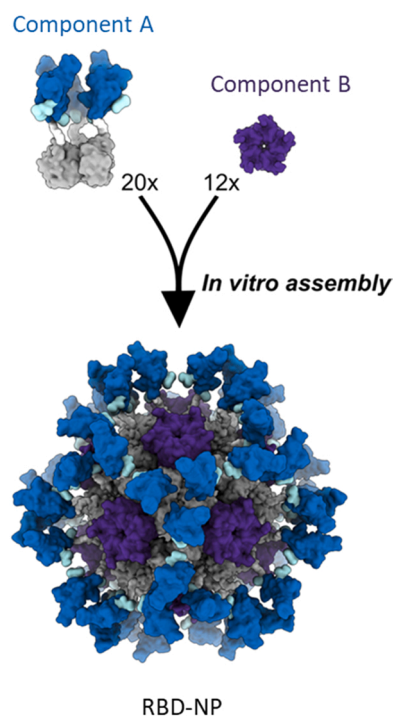


Fig. 1. Schematic of final assembly RBD nanoparticle, in vitro assembly, achieved by mixing Component A and Component B in a 1:1 molar ratio (monomer:monomer). The RBD of the SARS-CoV-2 spike protein is shown in blue, the 16-residue GlySer linker connecting it to the I53–50A trimer in white, the I53–50A trimer in gray, and the I53–50B pentamer in purple.

to generate cGMP Component A in support of clinical development of the RBD nanoparticle vaccine (RBD-NP) at Icosavax, Inc.

Process development (PD) activities at Amgen focused on developing a robust and reproducible manufacturing process for Component A (Fig. 1) including further development of analytical assays demonstrating successful nanoparticle assembly. Exploratory bench-scale PD studies were conducted at the IPD for both Component A and Component B. IPD provided Component B to support analytical assay development at Amgen. In response to the pandemic, to accelerate entry into the clinical trials, in addition to using a transient cell line for early PD, a stable cell pool instead of a clonal cell line was used for First-in-human (FIH) Component A production. These strategic changes enable a 2–3-month time saving, normally associated with cloning, clone screening, and selection activities. This time savings afforded opportunities to conduct thorough purification and analytical method development in addition to Drug Substance Intermediate (DSI) stability and viral clearance studies. Here we describe an accelerated six-month process development cycle, from vector construction to completion of investigational new drug (IND) enabling documentation.

2. Materials and methods

2.1. Plasmid construction

The coding sequence for Component A received from the IPD was modified before being cloned into a proprietary mammalian expression vector. The modifications include removal of a 12 bp overhang at the beginning of the mature peptide and the 8xHis tag plus its linker. Four plasmid sets were constructed using two signal peptides (one is murine phosphate, and the other is VK1) and two codon sets (one is the original and the other with optimization performed on 138 bp from position 691 to position 828 and a codon change at A374 from GCC to GCT). The sequence was synthesized in two DNA fragments called gBlocks by an external gene provider. The DNA fragments were then amplified by PCR

primers to add a linker region and overhangs to facilitate ligation independent cloning.

2.2. Pool generation and banking

The cell lines producing Component A were generated by transfecting the plasmids described above into a dihydrofolate reductase (DHFR)-deficient Chinese hamster ovary (CHO) host. Six replicate pools were created per plasmid using a standard electroporation procedure. After transfection, these pools were passaged in selective media deficient in glycine, hypoxanthine, and thymidine (-GHT). Half of the generated pools were cultivated in a humidified incubator (Kuhner AG, Basel, Switzerland) with 5% CO₂ and kept at 32 °C, while the other half were kept at 36 °C. Viable cell density, viability, and population doubling time were monitored until high viability was reached (> 80%). After pool evaluation in a small-scale fed-batch production (described in Section 2.3), a master cell bank was generated from the highest performing pool, which was subsequently used for clinical production.

2.3. Small-scale fed-batch production

A 50 mL Spin-Tube model (TPP, Trasadingen, Switzerland) was used to assess the performance of the recovered pools in a 10-day fed-batch assay using proprietary chemically defined medium. For all conditions, 20 mL cultures were cultivated in a humidified incubator (Kuhner AG, Basel, Switzerland) with 5% CO₂ at 36 °C. The cells were inoculated at 8×10^5 cells/mL and fed on days 3, 6 and 8. Viable cell density, viability, and cell diameter were measured using a Vi-Cell XR (Beckman Coulter, Fullerton, CA) while metabolites including glucose were measured by Bioprofile Flex Analyzer (Nova Biomedical, Waltham, MA). Day 10 cell culture supernatants were analyzed for titer and product quality.

2.4. Upstream process development

Stable CHO cell pools expressing Component A were cultured in shake flasks during seed train expansion using a proprietary selective medium. Component A material was generated using a fed-batch 50 L bioreactor incubated for 11 days. The culture was fed a defined amount of a proprietary chemically defined medium on specific days. Temperature set point and agitation were controlled by distributed control units. pH set point was maintained through addition of carbon dioxide and a liquid base solution. Dissolved oxygen was maintained through sparging of air and oxygen into the reactor. Cell cultures were harvested either through centrifugation and sterile filtration or depth filtration and sterile filtration prior to purification.

Viable cell density (VCD, measured using Cedex HiRes Analyzer, Roche CustomBiotech, Penzberg, Germany), metabolites (measured using Cedex Bio Analyzer and Cedex Bio HT Analyzer, Roche Custom-Biotech, Penzberg, Germany), osmolality (measured using OsmoTECH PRO Multi-Sample Micro-Osmometer, Advanced Instruments, Norwood, MA), titer (measured through HIC-HPLC analysis), and packed cell volume (PCV) were analyzed throughout the duration of cell culture.

2.5. Downstream process development

Early purification activities were supported by Component A material generated using a transient HEK293 expression system. Process confirmation and robustness studies were subsequently performed using material sourced from 50 L material supplies generated using stable pools. Representative in-process pools were leveraged to execute a preliminary viral clearance assessment, to address scale-up challenges like depth filtration fouling, and to towards yield improvement and robustness studies. Lastly, GMP in-process materials were used for filed viral clearance studies.

Chromatography purification steps were developed using the ÄKTA

Avant 150 and ÄKTA pilot 600S chromatography systems (Cytiva, Massachusetts, USA), and process filtration steps were developed using multilayer diatomaceous earth and cellulose based Millistak+® depth filters from MilliporeSigma (Millipore Corporation, Darmstadt, Germany). Evaluated depth filters have the following nominal micron rating (μm): X0HC ($< 0.1 \mu\text{m}$), F0HC ($< 0.4 \mu\text{m}$), A1HC ($< 0.5 \mu\text{m}$), C0HC ($0.2 - 2 \mu\text{m}$), and D0HC ($0.6 - 9 \mu\text{m}$) [11]. Filtration pressure profiles were monitored using a PendoTECH® pressure monitoring and transmitting system (PendoTECH, Princeton, USA). Product quality was monitored using size exclusion ultra-high performance liquid chromatography (SE-UHPLC) and reduced capillary electrophoresis-sodium dodecyl sulfate (rCE-SDS), for high-molecular weight and fragments, respectively. Product titer was measured by hydrophobic interaction chromatography (HIC) purification. Process-related impurities such as host DNA and CHO host cell protein (HCP) were monitored using quantitative Polymerase Chain Reaction (qPCR), and enzyme-linked immunosorbent assay (ELISA), respectively.

2.6. Viral clearance assessment

As a new process and modality, the preliminary viral clearance assessments were conducted to estimate the overall process viral clearance capabilities for the Component A process using quantitative reverse transcription of polymerase chain reaction (RT-qPCR) assay for log reduction values (LRV) calculation. The filed viral clearance data package used representative GMP material and qualified small-scale models to evaluate the Component A purification process viral clearance capabilities supported by the median tissue culture infectious dose (TCID₅₀) assay where Xenotropic Murine Leukemia Virus (xMuLV) and Mouse Minute Virus (MMV) were used as model viruses.

The quantitative reverse transcription of polymerase chain reaction (RT-qPCR) and the median tissue culture infectious dose (TCID₅₀) assays were used to determine the virus titer present in each step. In addition, the numeric value of the amount of virus present in each sample was used to calculate the LRV at each unit operation using each model virus (Eq. (1)). Studies in both phases were performed in duplicate.

$$\text{Virus LRV} = \log_{10} \left(\frac{\text{Input Virus Load}}{\text{Output Virus Load}} \right)$$

Equation 1: Virus log reduction value (LRV).

2.7. Analytical methods

The concentrations of Component A in cell culture supernatants were determined by a hydrophobic interaction chromatography (HIC) method. Cell culture supernatants were purified via affinity chromatography (Atoll GmbH, Weingarten, Germany) for product quality analysis by size exclusion chromatography and reduced capillary electrophoresis using sodium dodecyl sulfate (rCE-SDS).

2.8. Hydrophobic Interaction Chromatography (HIC) assay development

2.8.1. Reference standard sample preparation

Component A reference standard was diluted to 1 mg/mL with 50 mM Tris, 150 mM NaCl, 100 mM Arginine, 5% sucrose, pH 8.0 (Component A formulation buffer). Upon dilution, Component A reference standard concentration was measured and used for calibration curve calculation. Prior to HIC method analysis, the diluted reference standard was further diluted at 1:1 dilution ratio with 1 M Ammonium Sulfate, 20 mM Sodium Phosphate, pH 6.5 (Component A sample dilution buffer).

2.8.2. In-process sample preparation

To prepare Component A in-process samples for HIC analysis, samples were first filtered through a 0.20 μm filter or centrifuged for 5 min

at approximately 12,000 rpm. If centrifuging, the supernatant of the in-process samples was carefully transferred into a micro centrifuge tube. The filtered in-process samples or supernatant were diluted at 1:1 dilution with Component A sample dilution buffer prior to HIC analysis.

2.8.3. In-process sample titer analysis

Component A HIC method employs a HIC HPLC column (Waters® Protein-Pak Hi Res HIC, 2.5 μm pore, 4.6 \times 35 mm PN: 186007582) using mobile phase A: 2 M Ammonium Sulfate, 20 mM Sodium Phosphate, pH 6.5 and mobile phase B: 20 mM Sodium Phosphate, pH 6.5. The gradient (hold 100% A for 2 min, then increase to 100% B for 20 min with gradient slope of 5% B/min) was performed at 0.5 mL/min. The chromatogram was monitored by UV light absorbance at 280 nm.

2.8.4. Calibration curve and in-process sample titer determination

Component A in-process sample titer is determined by comparing against the calibration curve of Component A reference standard (Section 2.8.1). The five-point calibration curve of the HIC method is established by loading the reference standard at 0.625 μg , 1.275 μg , 2.5 μg , 7.5 μg and 15 μg , respectively. The injection volume of each calibration point is calculated using the half of Component A reference standard concentration upon formulation buffer dilution (Section 2.8.1). A graph of the main peak area for each standard injection as a function of injection amount is plotted to generate a calibration curve.

The target loading of in-process sample after the preparation (Section 2.8.2) is 2.5 μg based on the estimated concentration. The actual loading of in-process sample between 0.625 μg and 15 μg is acceptable. The main peak of Component A in-process sample is identified by the comparison of the sample retention time to that of the standard. The in-process sample concentration is calculated using Equation 2.

$$\text{Concentration (mg/mL)} = \frac{A-b}{m} \times \frac{D}{V}$$

Equation 2: In-process sample concentration.

where: A = main peak area.

b = y-intercept.

m = slope.

D = dilution factor (D=2).

V = injection volume.

2.9. Potency binding assay development

Component A dilutions (20 μL) over the range of 3000 to 0.786 ng/mL were incubated with 20 μL of recombinant human biotinylated ACE2 (ACE2-biotin) (Acro BioSystems) at 80 ng/mL, 20 μL of recombinant SARS-CoV-2 (COVID-19) S protein RBD, Fc Tag (Spike RBD-Fc) (Acro BioSystems) at 40 ng/mL, and 40 μL of the AlphaScreen® General IgG (Protein A) Detection Kit containing Streptavidin donor beads and Protein A acceptor beads (PerkinElmer) at 0.01 mg/mL in half area 96-well plates (Corning). Binding assays were performed using the following assay buffer: 25 mM HEPES, 0.1 M NaCl, 0.2% BSA, pH 7.4. The total volume in each well was uniform at 100 μL per well. Plates were incubated for 2–4 h at ambient temperature before reading on an EnVision® (PerkinElmer) plate reader.

2.10. Glycan characterization

2.10.1. Sample preparation

Glycans on Component A GMP lot was characterized by LC-MS/MS peptide mapping using Endoproteinase Glu-C (Glu-C) and trypsin followed by Glu-C proteases. To reduce disulfide bonds, sample was treated with 8 mM dithiothreitol (DTT, Sigma-Aldrich, St. Louis, MO) at 37 °C for 30 min in a denaturing solution containing 6.4 M guanidine hydrochloride (Sigma-Aldrich, St. Louis, MO), 0.2 M Tris pH 7.5 and 2 mM EDTA. Following reduction, sample was alkylated with 14 mM iodoacetic acid (Sigma-Aldrich) at 25 °C for 25 min in dark. Alkylation was quenched with 6 mM DTT. Reduced alkylated sample (~ 1 mg/mL

protein concentration) was buffer exchanged to 0.1 M Tris, pH 7.5 containing 50 mM methionine using Bio-Spin 6 columns (Bio-Rad, Hercules, CA) according to the manufacturer's recommended procedure. After buffer exchange, the sample was aliquoted in two separate vials, into which an appropriate amount of Glu-C or trypsin (Roche, Sigma-Aldrich) was added separately to achieve an enzyme:substrate ratio of 1:10. Glu-C digestion was carried out at 37 °C for 4 h. Trypsin digestion was carried out at 37 °C for 1 h. After trypsin digestion, an appropriate amount of Glu-C was added to achieve an enzyme:substrate ratio of 1:10, followed by incubation at 37 °C for an additional 3 h. Each digest was quenched by adding an equal volume of 0.25 M acetate buffer (pH 4.8) in 8 M guanidine hydrochloride.

2.10.2. LC-MS/MS data collection

Each proteolytic digest was analysed by reversed phase liquid chromatography on an Agilent 1290-II HPLC directly connected to a Thermo Scientific Q-Exactive HF (Glu-C digest) or QE Biopharma high-resolution mass spectrometer (trypsin+ Glu-C). Peptides from Glu-C digest were eluted using Water's Acquity Peptide BEH C18 column (2.1 × 150 mm, 1.7 μm particle) at a flow rate of 0.25 mL/min with the column temperature maintained at 50 °C. Mobile phase A was 0.02% TFA and 0.1% (v/v) formic acid in water, and mobile phase B was 0.02% TFA and 0.1% (v/v) formic acid in acetonitrile (ACN). After an initial hold at 0.5% B for 7 min, mobile phase B was increased linearly to 35% in 70 min. Column wash was achieved by increasing mobile phase B to 90% in 5 min with hold for 3 min. Column was equilibrated with 0.5% B for 14 min. Peptides from trypsin + Glu-C digest were eluted using a Water's Acquity Peptide CSH C18 column (2.1 × 150 mm, 1.7 μm particle, 130 Å pore size) at a flow rate of 0.25 mL/min and a column temperature of 50 °C. Mobile phase A was 0.1% (v/v) formic acid in water, and mobile phase B was 0.1% (v/v) formic acid in acetonitrile. After an initial hold at 0.5% B for 5 min, the mobile phase B was increased linearly to 36% in 72 min. Column wash was achieved by increasing the mobile phase B to 90% in 2 min with hold for 5 min. Column was equilibrated with 0.5% B for 14 min.

The mass spectrometer was set up to collect a high-resolution MS full scan at resolution setting of 120,000 and AGC target of 1E6, followed by five or eight data-dependent higher-energy collision dissociation (HCD) MS/MS (normalized collision energy = 27%), with dynamic exclusion, of the most abundant ions.

2.10.3. Data processing

LC-MS/MS data were processed on MassAnalyzer [12], a custom program developed in-house (available in Biopharma Finder from Thermo Fisher Scientific). MassAnalyzer performs automated component detection [12], retention time alignment [13], peptide identification and glycan profiling in a fully automated fashion. It identifies glycopeptides containing different glycoforms by comparing experimental MS/MS to predicted MS/MS and determines the relative abundance of each glycoforms using signal intensities of each glycopeptide [14]. Glycans commonly observed in CHO-expressed proteins were included in the search. It has been demonstrated that glycan profiles determined by LC-MS on glycopeptide level are comparable to those determined by conventional approaches [15].

2.11. Purification of Component B

Briefly, research-use plasmids were synthesized by GenScript into pET29b- with a double-stop codon just before the C-terminal poly-histidine tag. GMP research-grade material was purified from inclusion bodies (IB) after microbial *E. coli* fermentation. Cell pellets were resuspended in PBS, homogenized, and then lysed by microfluidization, using three discrete passes. Following clarification by centrifugation, the supernatant was discarded, and inclusion bodies were extracted after using a series of two washes. The first wash involved PBS with the addition of 0.1% Triton X-100, and the second wash involved PBS with 1 M NaCl.

The addition of these two washes in series prior to extraction demonstrated the best clearance factor in removing HCP and endotoxin. After the IB washes, the protein was extracted from the pellet in PBS with the addition of 2 M urea and 0.75% CHAPs (3-[(3-Cholamidopropyl)dimethylammonio]-1-propanesulfonate).

After extraction, the sample was carried forward to DEAE Sepharose Fast Flow (FF) chromatography, following dilution with PBS to ensure binding to the resin. After binding to the DEAE column, subsequent washes with PBS + 0.1% Triton X-100, followed by a wash with PBS + 0.75% CHAPs in series, were demonstrably the most efficient combination evaluated for further removal of endotoxin from the sample. Elution of the pentamer was accomplished with PBS containing 500 mM NaCl. This buffer was suitable for final vialing and storage.

2.12. Size exclusion ultra high-performance liquid chromatography (SE-UHPLC) release and stability assay for assembled nanoparticle

2.12.1. Nanoparticles

The nanoparticle SEC method uses an Agilent BioSEC-5 column, 1000 Å, 5 μm, 4.6 mm × 150 mm (Agilent Part Number 5190–2539) on a Waters UHPLC system with UV detection at 220 nm. The mobile phase is 100 mM sodium phosphate, 250 mM sodium chloride, 5% (v/v) 2-Propanol at pH 6.8. The target injection load of the assembled nanoparticle is 6 μg, and the total run time of the method is 9 min at a mobile phase flow rate of 0.4 mL/min.

2.12.2. Size Exclusion Chromatography – Light Scattering (SEC–LS)

Size exclusion chromatography coupled to a multiple-angle laser scattering experiments were performed at 25 °C using a static light scattering detector DAWN™ HELEOS and Optilab® T-REX refractive index monitor (Wyatt Technology, CA, USA) coupled in-line to an Agilent 1200 series LC system (Hewlett Packard, USA), which consisted of a G1310A pump, a G1379B degasser, a G1365B diode-array detector and a G1329A autosampler. 300 μg of sample was injected into a Tosoh Biosciences TSKGel 3000SWXL Aggregate (ID 7.8 × 30 mm) size exclusion column. 100 mM phosphate, 250 mM NaCl, pH 6.8 was used as the mobile phase at a flow rate of 0.5 mL/min. Data analysis was performed using Astra v7 using the RI detector as the concentration source. Normalization, alignment, and band broadening were applied to the raw data and a dn/dc value of 0.185 was used for the calculation of the molecular weight [16].

2.12.3. Sedimentation Velocity Analytical Ultracentrifugation (SV-AUC)

SV-AUC analysis was performed on a Beckman Coulter ProteomeLab XL-I instrument at 18,000 rpm and the absorbance at 280 nm were recorded. Experiments were performed in double-sector centerpiece cell assemblies with quartz windows. Scans were collected at 20 °C. The SV-AUC data was analyzed using SEDFIT v16.36. In the analysis, the frictional ratio, time invariant noise, and meniscus values were allowed to float during the nonlinear least squares fit. Density and viscosity of the buffer was measured using a DMA 4500 (Anton Paar) densitometer and an AMVn (Anton Paar) viscometer, respectively.

2.13. Stability assessment of Component A

Previous excipient screening efforts identified a frozen liquid formulation for Component A consisting of 5 mg/mL Component A formulated with 50 mM Tris, 150 mM NaCl, 100 mM arginine, 5% sucrose, pH 8.0. The stability study was designed to evaluate the stability of the Component A at the recommended storage condition (RSC) of –70 °C. Additionally, the accelerated storage conditions (ASC) of –30 °C, 5 °C, and the stressed storage condition (SSC) of 25 °C were also evaluated to support handling and possible excursions. The formulation effectiveness and suitability were verified to minimize degradation that may occur during storage. The attributes and corresponding analytical methods used to assess the stability of the

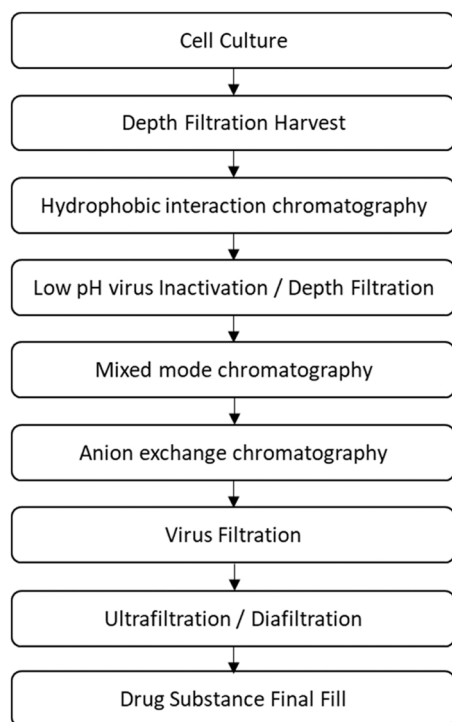


Fig. 2. Component A drug substance process flow diagram.

formulation included main peak by SE-UHPLC, nanoparticle assembly capability by SEC, purity by reduced CE-SDS, and potency by the binding assay.

3. Results

3.1. Development of stable CHO cell pools expressing Component A

The Component A Drug Substance process is shown in Fig. 2. Component A is produced from a stable CHO cell pool via fed-batch cell culture production followed by a depth filtration harvest, hydrophobic interaction chromatography capture step, a low pH viral inactivation, followed by a mixed mode chromatography and anion exchange chromatography polishing steps, into viral filtration and ultrafiltration/diafiltration (UF/DF), and then final filtration and fill.

To ensure robust expression of Component A in a stable CHO manufacturing cell pool, several modifications were made to the coding sequence for vector encoding Component A. First, a non-essential 12 bp overhang at the N terminus of the mature polypeptide (i.e., after signal peptide cleavage) and the 8xHis tag/linker were removed. Second, two different signal peptides (murine phosphatase and proprietary) and two codon sets (original and modified) were explored to improve expression of Component A in a DHFR-deficient CHO host. A total of 4 vectors were transfected in triplicate into CHO cells to generate pools (Fig. 3). During the cell line development (CLD) phase, the growth rate was also evaluated at both a lower temperature (32 °C) and the standard temperature (36 °C) for cell culture [3,9].

Fig. 3 shows the recovery profiles for all pools generated using the signal peptides and codon sets under different culturing temperatures. There was significant variability in pool recovery time depending on the temperature and the signal peptide used. All pools cultured at 32 °C or using the proprietary signal peptide (SP) failed to recover. Only six pools containing the murine phosphatase (MuP) signal peptide, either with or without codon modification, cultured at 36 °C recovered (> 80% viability).

All six recovered pools were cultured in small-scale fed-batch Spin-tubes to select the best pool for bioreactor production, based on titer

and cell culture growth. As shown in Fig. 4, five of six pools exhibited typical growth phenotype for this CHO host, with end viability around 60–80%. The normalized product titer of the pools measured by HIC-HPLC was in the range of 0.3–0.6 (Table 1), with 60–70% main peak as measured by SE-UHPLC, and 90% main peak as measured by rCE-SDS. Based on the cell culture performance in the Spin-tube small-scale fed-batch and the first material supply run, Pool 4 was selected as the final pool for Master Cell Bank (MCB) generation and subsequent clinical production. Standard clonal cell line activities were not pursued due to accelerated timelines in response to the pandemic.

3.2. Upstream process development

3.2.1. Material Supply 1

Material Supply run 1 was used to generate material for purification and analytical development, and to assist in selecting the lead candidate used for both non-human use (NHU) toxicology and clinical good manufacturing practice (GMP) lots. Three pools (4, 5, and 6) were selected for the secondary screen based on the small-scale fed-batch data discussed above. All three pools were run in 50 L bioreactors utilizing an 11-day fed-batch process with three bolus feeds.

Bioreactor cell culture performance is shown in Fig. 5. For cell growth, Pool 6 lagged significantly behind stable cell pools 4 and 5, with the maximum VCD being half that of any other pool. Pool 6 had the lowest final day viability as well as the highest lactate levels, resulting in a large consumption of base to maintain pH. The normalized titers for stable cell pools 4, 5, and 6 were 0.4, 0.2, and 0.5, respectively.

Given timeline constraints, the decision for the lead candidate was necessary on the final day of the Material Supply run 1, thereby allowing for the use of only bioreactor process data to decide the lead candidate. However, trends were consistent between the bioreactors and the small-scale fed-batch. Small-scale data indicated that Pools 4 and Pool 6 had higher titer than Pool 5. While Pool 6 had slightly higher titer compared to Pool 4, its poor cell culture growth and lactate metabolism would have resulted in potential process challenges as it progressed through manufacturing. Thus, Pool 4 was advanced as the top pool for master cell bank generation for the GMP run.

3.2.2. Material Supply 2

Material Supply run 2 provided process confirmation and material contingency. The lead CHO cell pool candidate (Pool 4) was produced in three bioreactors, with one bioreactor replicating the initial condition in Material Supply run 1, while the other two bioreactors employed a modified feeding schedule and two additional feeds. Due to the low ending viability observed in Material Supply run 1, these extra feeds were intended to improve the ending viability of the culture and potentially lead to increase in culture performance and titer. In addition, maintaining high viability through the end of the production run was hypothesized to help reduced HCP entering downstream processing.

Cell culture performance of Material Supply run 2 is shown in Fig. 6. Between the two fed-batch conditions, there were only slight differences towards the end of the production run, most notably a decrease in lactate levels and base consumptions using the modified condition. Due to the minimal impact of the additional feeds, this strategy was not further pursued. Material Supply run 2 utilized a depth filtration harvest. The yield of the depth filtration harvest step was approximately 75%, allowing for an effective harvest step that was implemented for subsequent lots. Normalized titer and product quality for Material Supply run 2, the NHU toxicology lot, and the GMP lot are summarized in Table 2.

3.3. Depth filtration development

During Component A process development, additional depth filtration development was needed to address low yield and throughput observed with more conventional depth filtration configurations for harvest and after low pH viral inactivation.

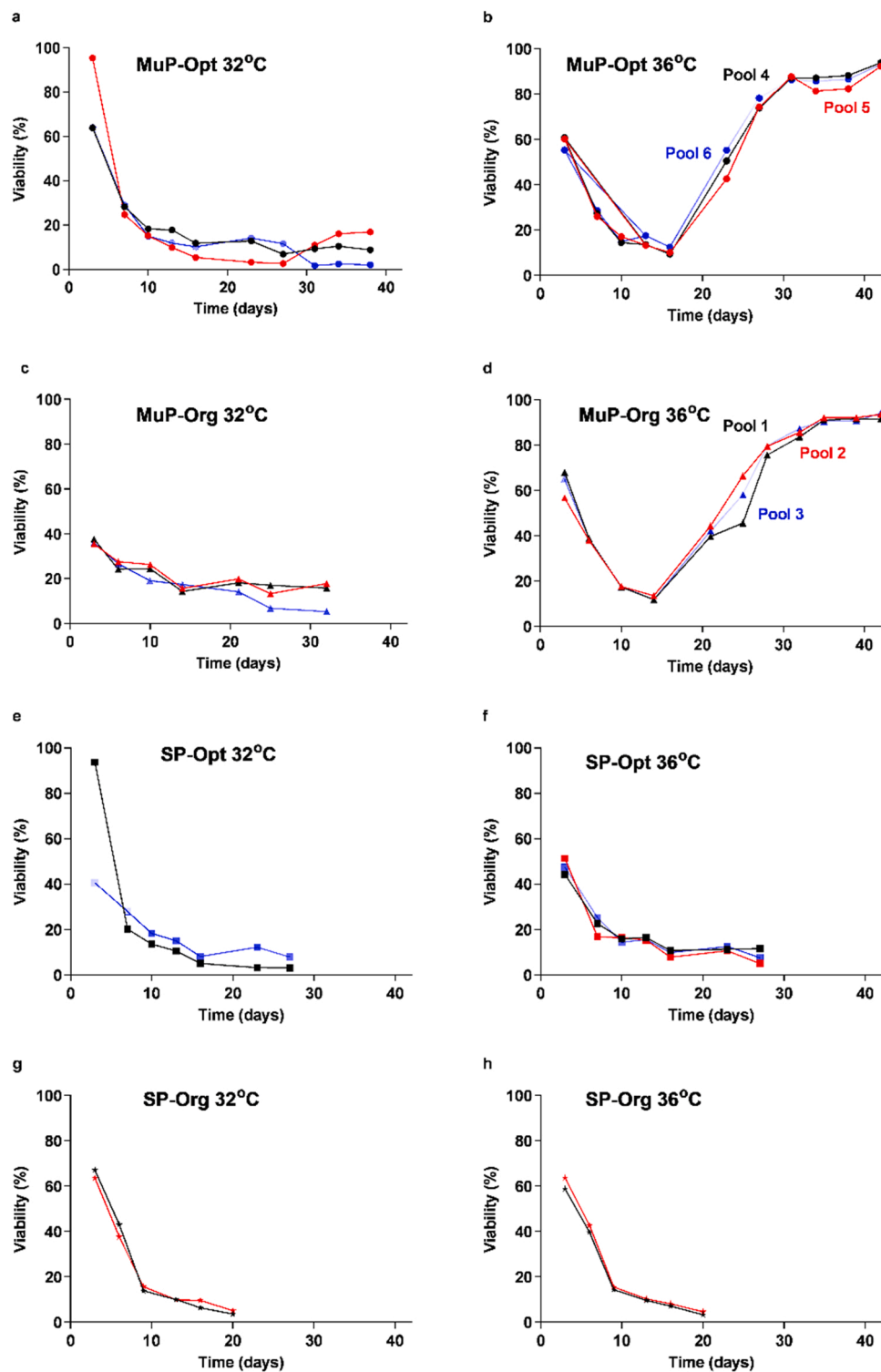


Fig. 3. Recovery profiles of all CHO-derived pools expressing Component A.

3.3.1. Harvest depth filtration

The objective of Study 1 was designed to assess preliminary stage 2 depth filtration throughput for FOHC, A1HC, and X0HC filters. A challenge cell culture supernatant with < 10% cell viability was intentionally generated to mimic a high cell debris stage 1 filtrate. With this challenge material, each filter achieved greater than or equal to 95 L/m² throughput. Surprisingly, this study also revealed an intrinsic 11–14 g/m² product loss during depth filtration which provided evidence that higher depth filtration throughput could be used to improve overall

process productivity. Based on recommendations from the external partner, the A1HC filter media was selected for subsequent studies.

Next, Study 2 was designed to assess Clarisolve 20MS, D0HC, and C0HC filters for stage 1 clarification in the depth filtration train. The previous challenge cell culture supernatant was leveraged, this time spiked with a 1×10^6 cell/mL VCD to mimic high viability at the end of production. As would be expected given its larger pore size, the Clarisolve 20MS provided a significantly higher throughput (67 L/m²) than both the D0HC and C0HC filter media (both < 20 L/m²). Therefore, the

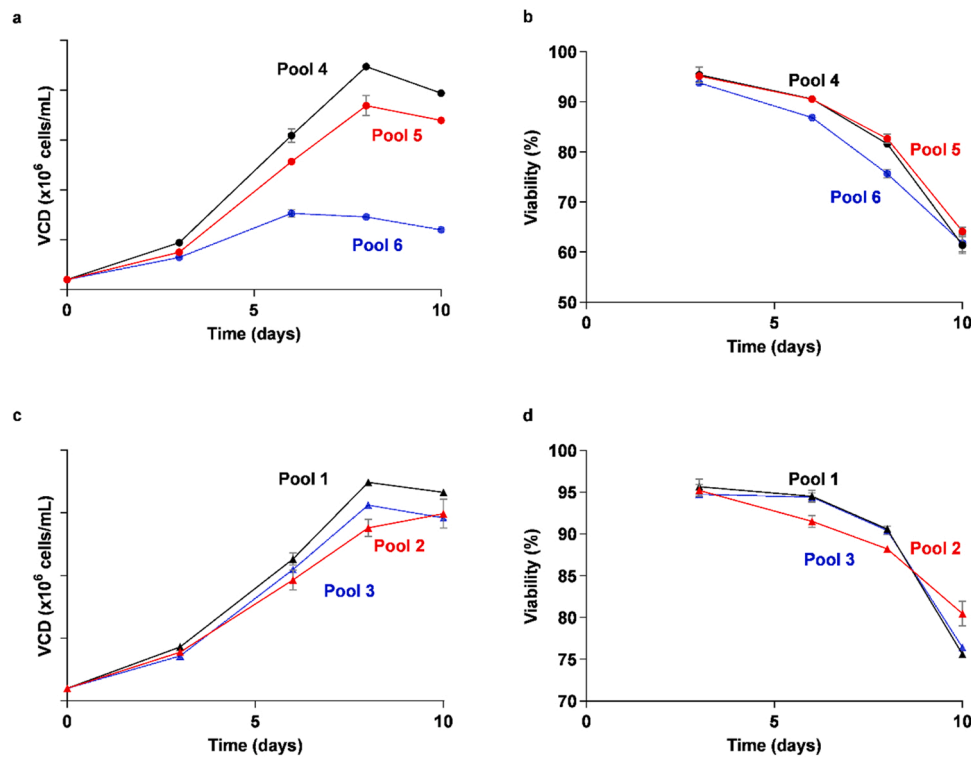


Fig. 4. Performance of CHO-derived pools expressing Component A in small-scale fed-batch. a) Viable cell density (VCD) for pools with modified codons, b) Viability for pools with modified codons, c) Viable cell density (VCD) for pools with original codons, d) Viability for pools with original codons.

Table 1

Productivity and product quality of CHO-derived pools expressing Component A in small-scale fed-batch.

Key indicator	Modified codons			Original codons		
	Pool 4	Pool 5	Pool 6	Pool 1	Pool 2	Pool 3
Normalized titer	0.6	0.3	0.5	0.6	0.6	0.6
SE-UHPLC main peak (%)	70.5	66.1	76.4	63.2	61.2	60.7
rCE-SDS main peak (%)	90.4	87.8	92.7	91.5	92.7	91.4
Relative potency (%)	60	50	64	N/A	N/A	N/A

Clarisolve 20MS filter was pursued as the stage 1 depth filter.

Finally, the objective of Study 3 was designed to confirm the harvest depth filtration train using representative materials and assess whether a harvest treatment step could be included to improve yield. For this study a Clarisolve 20MS filter was replaced with a Clarisolve 40MS filter due to a global shortage of bench scale Clarisolve 20MS filters but would

beneficially provide a challenge condition for the A1HC filter. The study determined that the A1HC filter could achieve a throughput of 183 L/m² which met the performance target. Cell culture broth acidification to pH 6.0 was also assessed but was found to significantly decrease the A1HC filtration throughput (73 L/m²), likely due to increased DNA and HCP aggregation and particle formation, based on the observation of increased turbidity. Therefore, culture broth acidification was not pursued. The results of these studies are summarized in Table 3.

3.3.2. NVIP depth filtration

Due to an unexpected and significant difference between the Material Supply run 2 and toxicology depth filtration throughput, a head-to-head comparison was performed on the neutralized virus inactivation pool (nVIP) using the FOHC and A1HC filters. Initially it was hypothesized that fouling during the toxicology campaign was due to the integrated 0.1 μm filter associated with the A1HC filter, which is absent in the FOHC. The Study 1 results however revealed that the throughput differences were related to differences in load material. The Material Supply run 1 achieved a significantly higher throughput (100–104 L/m²) than the toxicology material (18–22 L/m²) with both filters. These

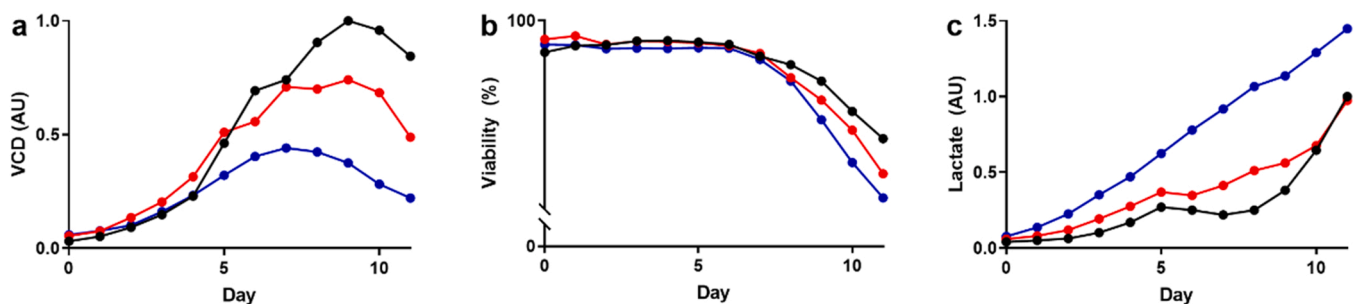


Fig. 5. Material Supply run 1 process data. Pools 4 (black), 5 (red), and 6 (blue) visualizing (a) viable cell density (VCD), (b) viability, and (c) lactate. VCD and lactate data is normalized to Pool 4.

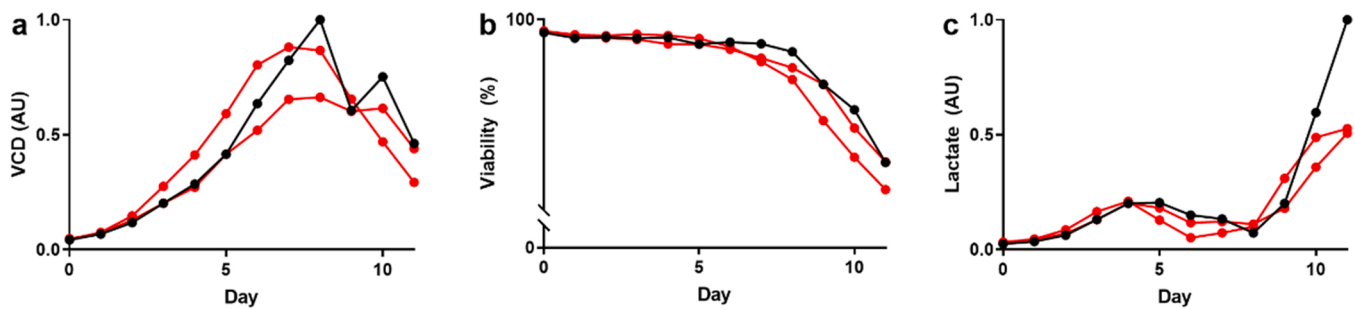


Fig. 6. Material Supply run 2 process data. Using Material Supply run 1 protocol (black) and protocol with additional feeds (red) visualizing (a) viable cell density (VCD), (b) viability, and (c) lactate. VCD and lactate data is normalized to the initial condition.

Table 2

Final day bioreactor and harvest material normalized titer and product quality for bioreactor Supply run 2, NHU toxicology and GMP campaign.

Key indicator	Final day bioreactor			Harvest material		
	Material Supply 2	NHU toxicology	GMP campaign	Material Supply 2	NHU toxicology	GMP campaign
Normalized titer	0.7	0.5	0.6	0.5	0.3	0.4
SE-UHPLC main peak (%)	66.6	57.1	57.0	66.6	58.0	54.5
rCE-SDS main peak (%)	85.0	78.5	80.2	81.0	72.3	77.6
HCP (ng/ug)	4301	4352	5540	3100	2306	6559
DNA (pg/ug)	18,635	23,692	23,028	9461	6414	9952

Table 3

Harvest development study results.

Study Block	Setup	Load Material	Flux (LMH)	Throughput (L/m ² at 25 psi inlet)
3	Clarisolve 20MS to A1HC (2:1)	Cell Broth	50	244
	A1HC	Clarisolve 40MS filtrate	50	183
2	Clarisolve 20MS	Challenge cell broth	50	67
	D0HC	Challenge cell broth	50	< 20
	COHC	Challenge cell broth	50	< 20
1	F0HC	Centrifuge Supernatant	50	107
	A1HC	Centrifuge Supernatant	50	108
	X0HC	Centrifuge Supernatant	50	95

Table 4

Depth filtration study results.

Study Block	Setup	nVIP material	Load Material	Flux (LMH)	Throughput (L/m ² at 35 psi inlet)
3	DOHC	NHU toxicology	Post run hold-up	70	196
	F0HC	NHU toxicology	Post run hold-up, DOHC Pool	70	> 190
2	COHC to F0HC	NHU toxicology	Post run hold-up	70	53
1	F0HC	Material Supply 1	Fresh	70	104
	F0HC	NHU toxicology	Post run hold-up	70	18
	A1HC	Material Supply 1	Fresh	70	100
	A1HC	NHU toxicology	Post run hold-up	70	22

observations prompted additional process development to update the nVIP depth filtration process.

To improve throughput and robustness, subsequent studies evaluated options for two-stage depth filtration trains. For Study 2, a COHC and FOHC filters were placed in series and throughput was evaluated using material from the toxicology lot. The overall throughput was determined to be approximately 50 L/m², which was lower than the performance target. Pressure measurements at the inlet of both filters identified that the COHC filter was fouling first, suggesting that a larger pore size stage 1 filter was required.

For Study 3, a single DOHC depth filter was employed, and the resulting filtrate was then applied to a FOHC depth filter. The results revealed that a maximum throughput of 196 L/m² could be achieved with the single DOHC filter while the FOHC was able to achieve a maximum throughput of greater than 190 L/m² with the DOHC filtrate without exceeding safe operating pressure. Based on these results, the DOHC, FOHC, SHC filter train was implemented for the GMP run. The results of those studies are summarized in Table 4.

3.4. Purification development

The final purification process consists of three orthogonal chromatography steps, consisting of HIC, CHT and SPFF and includes low pH viral inactivation, viral filtration and UF/DF. Chromatography conditions were adapted from the IPD exploratory bench-scale studies, and confirmatory and optimization studies were conducted during and in parallel to the NHU toxicology run prior to the FIH GMP run. The following sections describe the most significant development activities involving the three chromatography steps.

3.4.1. Capture step using Hydrophobic Interaction Chromatography (HIC)

The product capture step is the first unit operation in purification, which is designed to recover the protein product from the harvested cell culture fluid (HCCF). Since the Component A construct does not contain an Fc or similar purification tag, ion exchange (IEC) and hydrophobic interaction (HIC) were considered suitable replacements. IPD first demonstrated that HIC could be used to capture Component A. Two resins were evaluated in an early assessment using transient HEK293 derived materials: Fractogel® EMD SO₃⁻ (M), a strong cation exchanger (CEX) resin, and Butyl Sepharose 4 Fast Flow, a standard aliphatic

Table 5
Capture step yields using several salt conditions.

Salt	Concentration	Conditioning ratio ^a	Step yield (%)
Sodium Chloride	2 M	60%:40%	15
	2.5 M	50%:50%	100
	3 M	40%:60%	89
Sodium Sulfate	0.75 M	50%:50%	100
	1 M	33%:67%	83
Ammonium Sulfate	0.5 M	50%:50%	74
	0.8 M	80%:20%	81
Sodium Citrate	0.6 M	60%:40%	14

^a X% part product (HCCF); X% part buffer diluent.

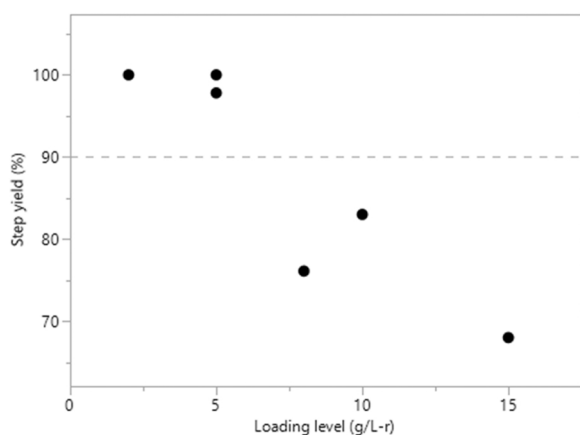


Fig. 7. Effect of loading level in step yield evaluation. The dash line indicates the desirable threshold of 90% step yield.

hydrophobic interaction chromatography (HIC) resin. The HIC resin exhibited better protein binding capacity compared to the CEX resin, therefore Butyl Sepharose 4 Fast Flow resin was selected for further capture development.

Hydrophobic interaction chromatography utilizes a high salt environment that exposes hydrophobic regions of proteins by reducing solvation. The high salt promotes the interaction between hydrophobic and hydrophilic regions of the medium and protein. Thus, several salts at different concentrations such as sodium chloride (2–3 M), sodium

sulfate (0.75–1 M), ammonium sulfate (0.5–0.8 M), and sodium citrate (0.6 M) were evaluated to determine the optimal HIC binding conditions. All buffer conditions were prepared using a 20 mM sodium phosphate background buffer. The criteria for final process conditions were based on 1) step yield, 2) manufacturability, and 3) facility fit.

2.5 M sodium chloride and 0.75 M sodium sulfate resulted in effective product binding, resulting in 100% step yield. Experiments with 3 M sodium chloride, 1 M sodium sulfate, 0.8 M and 0.5 M ammonium sulfate demonstrated acceptable performance. Alternatively, lower salt concentrations (2 M sodium chloride and 0.6 M sodium citrate) led to poorer product binding (Table 5). Finally, when comparing 2.5 M sodium chloride and 0.75 M sodium sulfate conditions, both conditions promoted adequate product binding, while also meeting product quality and step yield targets. Optimal product binding and yield was achieved with 20 mM sodium phosphate 2.5 M sodium chloride which was consistent with the IPD exploratory findings. In addition to process performance, sodium chloride was selected for being more environmentally friendly and cost-effective. Due to the relatively high density and salt concentration of the conditioning buffer, the batch conditioning was performed under slow addition, with gentle and thorough mixing instead of using an in-line operation to ensure consistent and reproducible product binding.

Next, protein loading levels (2–15 g/L of resin, g/L-r) and wash steps (0.9–1.8 M of sodium chloride) were evaluated as means to optimize recovery yield and product quality. As shown in Fig. 7, with respect to step yield, the optimal loading level was established to be ≤ 5 g/L-r which resulted in $> 90\%$ yield. Other loading levels at 8, 10, and 15 g/L-r led to lower step yields between 68% and 83%. Chromatography profiles in Fig. 8 confirm these findings, where 5 g/L-r loading resulted

Table 6

Process step yield and SE-UHPLC delta results using 2 mM and 10 mM sodium phosphate for load conditioning.

Key indicator	2 mM Sodium phosphate	10 mM Sodium phosphate
Delta ^a SE-UHPLC main peak (%)	+ 12.1	+ 13.9
Delta ^a SE-UHPLC HMW (%)	-3.4	-5.0
Delta ^a SE-UHPLC LMW (%)	-8.7	-9.0
Step Yield (%)	49.0	61.7

^a Difference of the elution pool results and the load results.

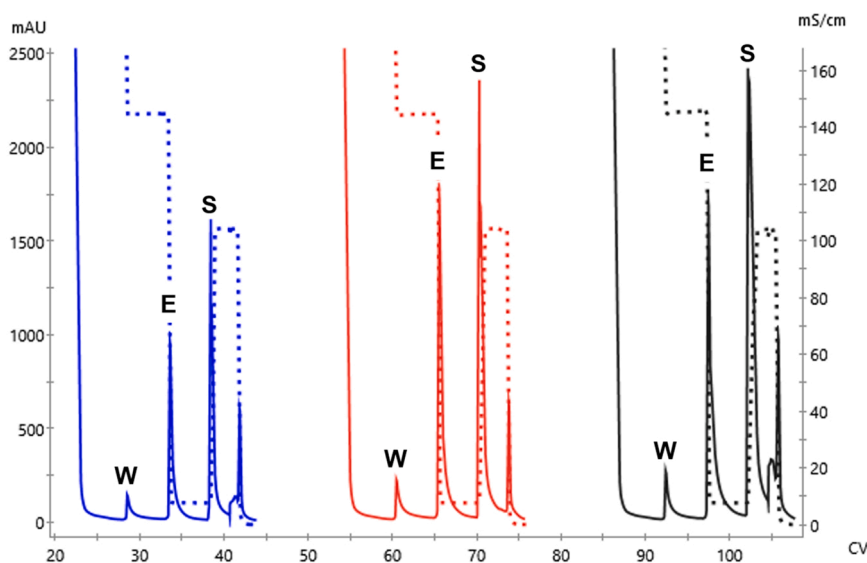


Fig. 8. HIC Chromatograms - loading level evaluation. Protein loading level (from left to right) 2 g/L-r (blue), 5 g/L-r (red) and 8 g/L-r (black); 280 mAU (—), Conductivity mS/cm (---), second wash peak using 20 mM sodium phosphate, 1.8 M sodium chloride (W), elution peak (E), strip peak (S).

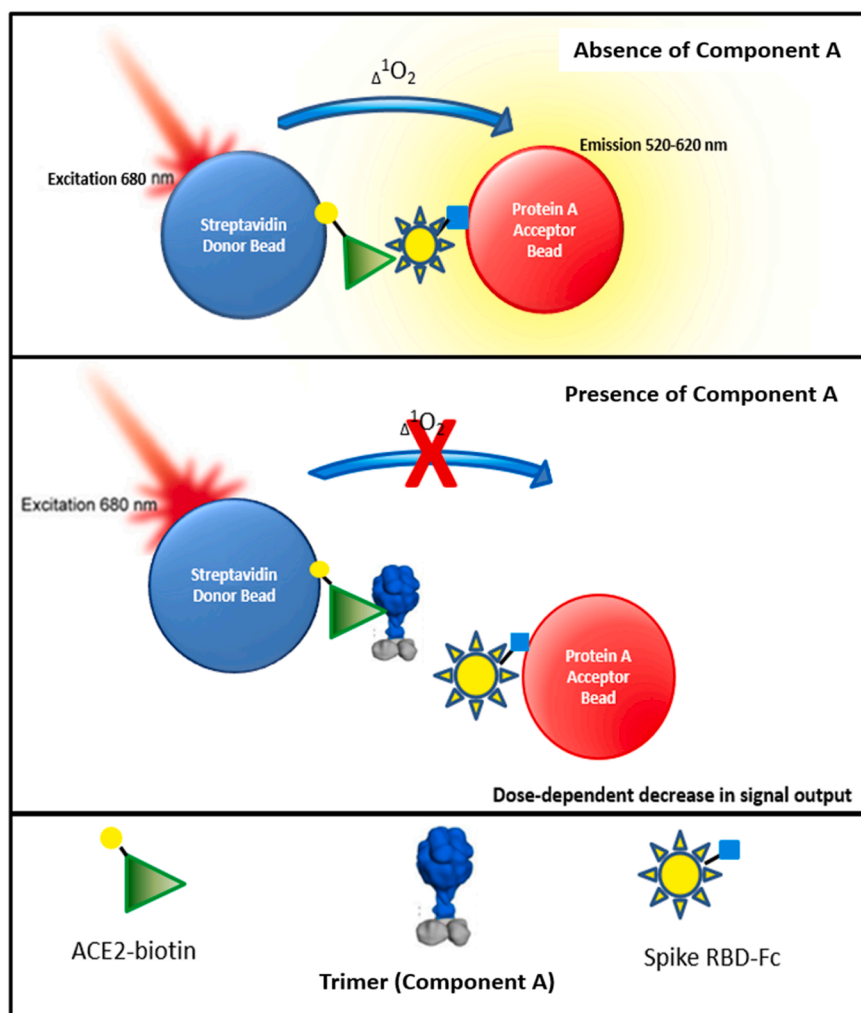


Fig. 9. Principle of the potency binding assay. When Spike RBD-Fc and ACE2-biotin bind to each other, the streptavidin donor beads, and the protein A acceptor beads are brought into close proximity. When a laser is applied to this complex, ambient oxygen is converted to singlet oxygen by the donor beads. If the beads are in close proximity, an energy transfer from the singlet oxygen to the thioxene derivative in the acceptor beads occurs, resulting in the production of luminescence. Component A binds to ACE2-biotin and prevents it from binding to Spike RBD-Fc, thereby decreasing the luminescence output in a dose-dependent manner.

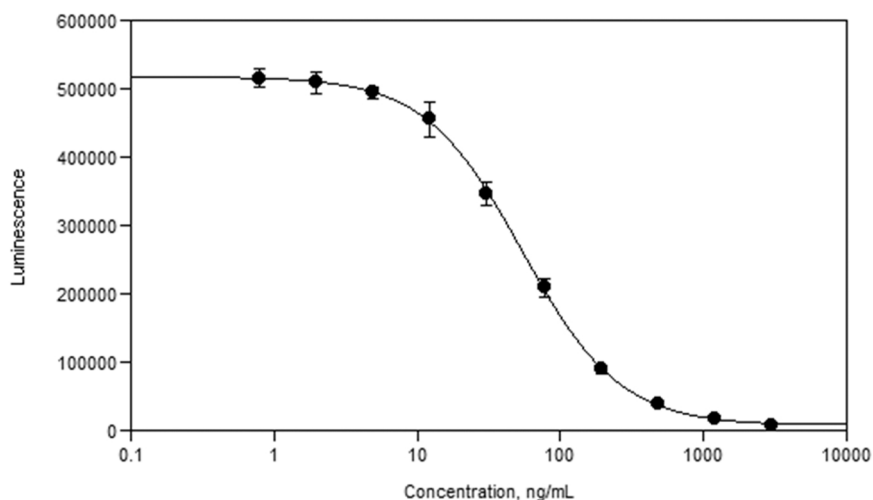


Fig. 10. Representative dose response curve in the potency binding assay. Increasing concentrations of Component A inhibit binding of ACE2-biotin to Spike RBD-Fc resulting in a dose-dependent decrease in luminescence.

in significantly less product lost in the strip phase, when compared to 8 g/L-r loading.

Since HIC can also nonspecifically bind process impurities like DNA and HCP, a second wash step was included to improve impurity clearance and product resolution. As expected, lower salt concentrations

significantly reduced yield, where 0.9 M and 1.2 M NaCl resulted in 69% and 61% yield, respectively. In contrast, higher salt concentrations (≥ 2 M sodium chloride) provided negligible DNA and HCP removal. It was determined that a 1.8 M sodium chloride wash was capable of providing additional process-related impurities clearance while maintaining high

Table 7

Glycans observed at site N331 in Glu-C digest (peptide RFPNITNLCPFGE).

Glycan ^a	Abundance
N331 + A1G0F	1.29%
N331 + A1G1F	2.01%
N331 + A1S1F	0.97%
N331 + A2G0F	2.27%
N331 + A2G1F	3.38%
N331 + A2G2F	5.22%
N331 + A2S1G0F	6.76%
N331 + A2S1G1F	20.23%
N331 + A2S2F	15.41%
N331 + A3G0F	0.77%
N331 + A3G1F	0.87%
N331 + A3G2F	1.07%
N331 + A3G3F	2.11%
N331 + A3S1G0F	1.09%
N331 + A3S1G1F	2.17%
N331 + A3S1G2F	7.30%
N331 + A3S2G0F	1.28%
N331 + A3S2G1F	7.65%
N331 + A3S3F	4.01%
N331 + GnF	0.37%
N331 + Unglycosylated	13.78%

^a Glycan nomenclature: Complex glycans are represented as AaSSgGF, where a represents number of antennas, s represents number antenna terminating with a sialic acid, g represents number of antennas terminating with a galactose, and F represent the presence of the core fucose. Gn represents a GlcNAc.

Table 8

Glycans observed at site N343 in trypsin+ Glu-C digest (peptide VFNATR).

Glycan ^a	Abundance	Glycan	Abundance
N343 + A1G0	0.37%	N343 + A2S1G1	0.07%
N343 + A1G0F	2.98%	N343 + A2S1G1F	15.45%
N343 + A1G0M4F	0.56%	N343 + A2S1G1M4F	0.09%
N343 + A1G0M5	0.08%	N343 + A2S2F	13.12%
N343 + A1G1	0.13%	N343 + A2S2M4F	0.07%
N343 + A1G1F	0.57%	N343 + A3G0F	2.47%
N343 + A1G1M4F	0.26%	N343 + A3G1F	2.14%
N343 + A1G1M5	0.09%	N343 + A3G2F	2.48%
N343 + A1G1M5F	0.04%	N343 + A3G3F	2.51%
N343 + A1S1	0.07%	N343 + A3S1G0F	1.13%
N343 + A1S1F	0.78%	N343 + A3S1G1F	1.89%
N343 + A1S1M4	0.11%	N343 + A3S1G2F	2.40%
N343 + A1S1M4F	0.27%	N343 + A3S2G0F	0.93%
N343 + A1S1M5	0.06%	N343 + A3S2G1F	1.56%
N343 + A2G0F	7.05%	N343 + A3S3F	0.60%
N343 + A2G1	0.09%	N343 + Gn	0.38%
N343 + A2G1F	9.97%	N343 + GnF	0.08%
N343 + A2G2	0.15%	N343 + M3	1.50%
N343 + A2G2F	13.13%	N343 + M4	0.27%
N343 + A2G2M4F	0.09%	N343 + M5	7.52%
N343 + A2S1G0F	6.86%	N343 + Unglycosylated	0.04%

^a Glycan nomenclature: Hybrid glycans are represented as AaSSgGmMmF, where a represents number of antennas, s represents number antenna terminating with a sialic acid, g represents number of antennas terminating with a galactose, m represents the number of mannose residues, and F represent the presence of the core fucose. Oligomannose glycans are represented as Mm, where m represents the number of mannose in the glycan.

overall step yield (Fig. 8).

3.4.2. First polishing step using Mixed Mode Chromatography (MMC)

The second chromatography step uses a mixed-mode chromatography (MMC) resin, CHT Ceramic Hydroxyapatite (Type I – 40 µm) which consists of spherical, macroporous hydroxyapatite, a form of calcium phosphate. The chromatography is operated in a bind and elute mode using a salt gradient elution. This polishing step is designed to

remove both process and product-related impurities. This resin was recommended based on IPD exploratory studies.

To ensure appropriate product binding conditions and to maximize the CHT resin lifespan, loading equilibration was evaluated first. A comparison between 2 mM and 10 mM sodium phosphate in the load material resulted in similar binding profiles (Table 6). However, the load material containing 10 mM sodium phosphate resulted in marginally higher main peak (%) by SE-UHPLC, and a 12.7% higher yield when compared to the 2 mM sodium phosphate condition. In addition to better performance, the 10 mM load condition also provided significantly better manufacturability, as it required 9 times less buffer to perform the conditioning and was therefore selected.

Finally, optimal protein loading was determined to be 5 g/L-r. Higher loading at 10 g/L-r resulted in greater low molecular weight (LMW) content in the elution pool.

3.4.3. Second polishing step using Anion Exchange Chromatography (AEX)

The third chromatography step used a strong anion exchange chromatography (AEX) Q Sepharose Fast Flow (QSFF), operated in flow-through mode. In addition to product resolution AEX generally provides significant viral clearance capabilities.

The AEX process was operated at 7.5 pH. Protein loading level was found to be optimal at ≤ 20 g/L-r which exhibited a robust step yield of 100% and with 97.4% main peak by SE-UHPLC and 93.0% main peak by rCE-SDS.

3.5. Analytical method development

The accelerated process development timeline for Component A drug substance intermediate necessitated creative approaches for analytical method development and qualification. Given the nature of the constructs and the lack of affinity tags, several product-specific analytical methods had to be employed. These included a HIC method to measure titer in cell culture, a bead-based binding assay to measure the relative potency of Component A, and a size-exclusion chromatography (SEC) based assay to quantify nanoparticle formation after the addition of Component B. Standard analytical methods to monitor critical product quality attributes such as aggregation (SE-UHPLC) and clipping (rCE-SDS) were also leveraged for Component A.

Analytical method development was initiated with research-grade Component A and Component B material procured from the IPD. After the method parameters and conditions were established, full method qualification was performed at risk with the research-grade material to meet the accelerated timelines. The suitability of the qualified methods was further confirmed by performing a limited method verification using representative material prior to lot release for Good Laboratory practice (GLP) toxicology studies. The agile approach to analytical method development was crucial for ensuring on-time readiness of release and stability methods for the GMP clinical lot of Component A.

In addition to the critical attributes monitored at release and stability per specifications, Component A was further characterized by mass spectrometry to map the complex glycan profile, and by light scattering and AUC to assess the higher order structure of Component A and the assembled nanoparticle. The totality of the analytical package demonstrated acceptable product quality for advancement of Component A drug substance intermediate to clinical trials.

3.5.1. Hydrophobic Interaction Chromatography (HIC)-based titer method development

Component A in-process titer was determined by comparing the sample against a calibration curve generated using a Component A reference standard injected at varying known loads on a HIC column. Key metrics were used to assess method performance during the development phase, sample binding affinity to the HIC column, and high protein recovery to achieve best accuracy of titer measurement. The following method parameters were evaluated using key metrics: 1)

Table 9
Schematic of glycans observed in Component A.

Short					
Gn		GnF			
Oligomannose					
M3		M4		M5	
Hybrid					
A1G0		A1G0F		A1G0M4	
A1G0M5		A1G0M5F		A1G1	
A1G1F		A1G1M4F		A1G1M5	
A1G1M5F		A1S1M4		A1S1M4F	
A1S1M5		A2G2M4F		A2S1G1M4F	
A2S2M4F					
Complex					
A2G0F		A2G1		A2G1F	
A2G2		A2G2F		A3G0F	
A3G1F		A3G2F		A3G3F	
Complex with sialic acid					
A1S1		A1S1F		A2S1G0F	
A2S1G1		A2S1G1F		A2S2F	
A3S1G0F		A3S1G1F		A3S1G2F	
A3S2G0F		A3S2G1F		A3S3F	
	GlcNAc		Mannose		Galactose
			Sialic acid		Fucose

sample dilution buffer composition, 2) mobile phase composition, 3) elution gradient, and 4) mobile phase flow rate. The final method parameters were recommended after a rigorous analysis of the method development data. The HIC method was subsequently qualified to be used in a GMP setting for in-process titer measurements during clinical manufacturing.

3.5.2. Potency binding assay development for Component A

The SARS-CoV-2 spike protein contains a receptor-binding domain

(RBD) that allows it to bind to the human angiotensin I-converting enzyme 2 (hACE2) receptor expressed on certain human cells, facilitating its entry. The assay for potency is therefore a binding assay.

The potency binding assay is a bead-based Amplified Luminescent Proximity Homogeneous Assay (Alpha) that detects biomolecular interactions. The assay contains two bead types: acceptor beads and donor beads. The donor beads are coated with a hydrogel that contains phthalocyanine, a photosensitizer and streptavidin. The acceptor beads are coated with a hydrogel that contains thioxene derivatives as well as

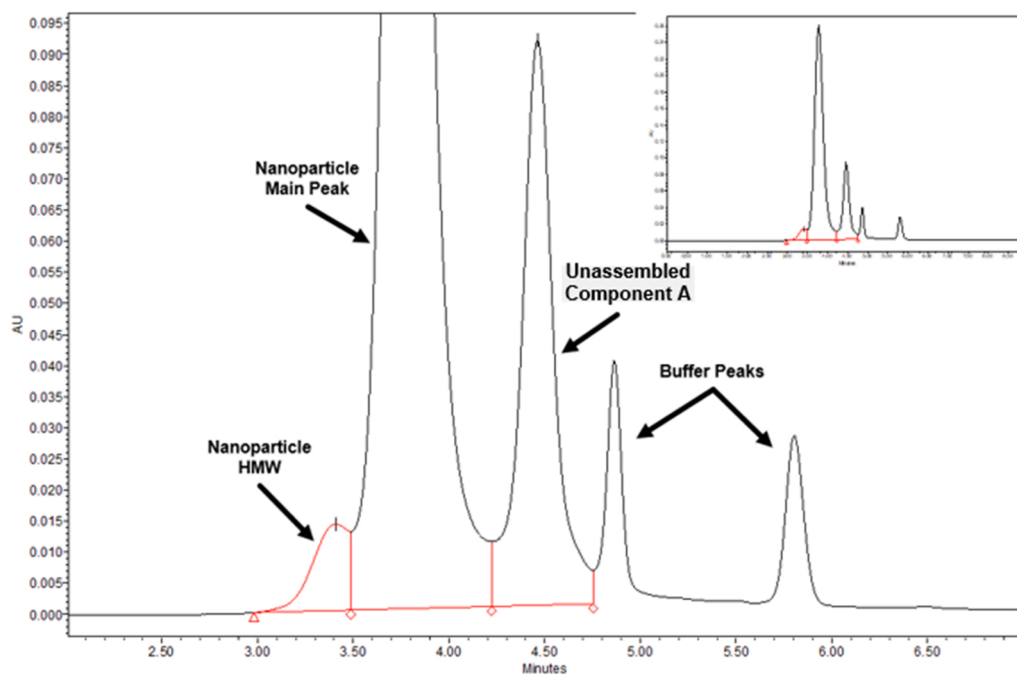


Fig. 11. Representative SE-UHPLC chromatogram of assembled vaccine nanoparticle.

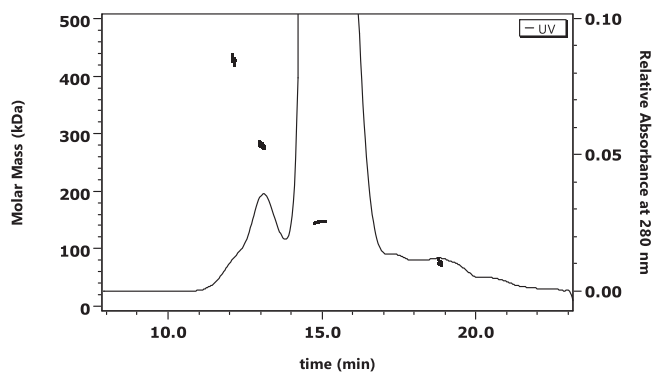


Fig. 12. Overlay of the molar masses of the trimeric Component A and its aggregates, and the UV chromatogram from SEC-LS analysis (10X Zoom).

Protein A. The donor beads bind to biotinylated ACE2 (ACE2-biotin) through interaction between streptavidin and biotin, while the acceptor beads bind to an Fc-tagged RBD of the SARS-CoV-2 spike glycoprotein (Spike RBD-Fc) due to the interaction between Protein A and Fc. When Spike RBD-Fc and ACE2-biotin bind to each other, the acceptor beads and the donor beads are brought into close proximity. When a laser is applied to this complex, ambient oxygen is converted to singlet oxygen by the donor beads. If the beads are in proximity, an energy transfer from the singlet oxygen to the thioxene derivative in the acceptor beads occurs, resulting in the production of luminescence, which is measured in a microplate reader equipped with AlphaScreen® signal detection capabilities. When Component A is added to the reaction mix, it binds to ACE2-biotin and prevents it from binding to Spike RBD-Fc, thereby decreasing the luminescence output in a dose-dependent manner. Test sample activity is determined by comparing the test sample response to that of a Reference Standard (relative potency). The principle of the potency binding assay is shown in Fig. 9 and a representative dose response curve is shown in Fig. 10.

3.5.3. Glycan characterization of Component A

Component A has two potential N-linked sites in close proximity,

N331 and N343 [17]. Accurate quantitation of the glycan profile on each site requires one site per peptide. To achieve this, two different digests were prepared. The automated data processing tool for glycan analysis in MassAnalyzer compares the experimental MS/MS to accurately predicted theoretical MS/MS of unmodified and modified peptides and generates a list of identified glycans with site specific information [14, 15]. Table 7 shows glycans observed at site N331 from Glu-C peptide (RFPNITNLCPFGE). The majority of glycans observed at site N331 are complex glycans including fucosylated biantennary and tri-antennary with varying amounts of galactosylation and sialylation. Oligomannose and hybrid type glycans are not observed at this site. Table 8 shows glycans observed at site N343 from trypsin + Glu-C peptide (VFNATR). This site shows the presence of complex, hybrid and oligomannose types of glycans. The major glycans observed at site N343 are fucosylated biantennary with varying amount of sialylation. Glycan occupancy at site N331 is ~86% while site N343 is almost completely occupied with glycans. Table 9 shows graphical presentation of glycans identified in Component A.

3.5.4. Characterization of assembled vaccine nanoparticles

3.5.4.1. Size Exclusion Ultra High-Performance Liquid Chromatography (SE-UHPLC)- based release and stability assay for assembled nanoparticle.

To demonstrate assembly competency of Component A, a size exclusion chromatography method was employed due to the dramatic difference in hydrodynamic radius between component and assembled nanoparticle. First, a small-scale assembly reaction using a 1:1 molar ratio of Component A to Component B (subunit:subunit) was performed. To generate sufficient quantities of Component B that could be used for test assemblies with the Component A RBD fusion protein after each unit operation, IPD developed and subsequently transferred a scale-up process for manufacturing Component B.

Following the assembly reaction, assembled nanoparticle was analyzed using SE-UHPLC and the differences in retention time were compared to quantitate the amounts of assembled nanoparticle, assembled nanoparticle aggregate, and unassembled Component A. Due to the large size of the assembled nanoparticle (~3.9 MDa), size exclusion columns with large pore sizes were screened, with a 1000 Å pore size providing the best resolution between the assembled nanoparticle

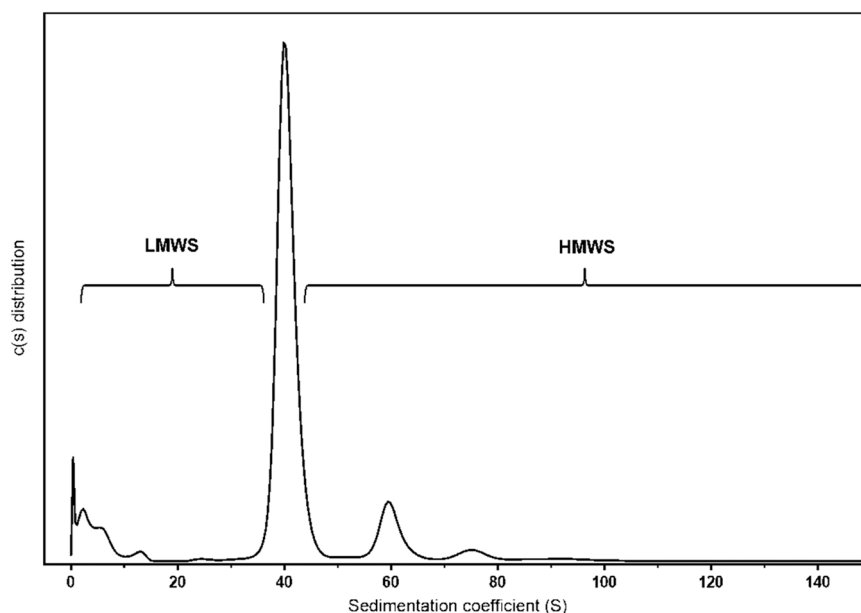


Fig. 13. Sedimentation coefficient distribution of nanoparticles formed by incubating Component A with Component B.

and unassembled components (Fig. 11). During development, non-specific interactions between the assembled nanoparticle and the size exclusion column were observed. To minimize these non-specific interactions, isopropyl alcohol was added to the mobile phase.

3.5.4.2. Size Exclusion Chromatography – Light Scattering (SEC-LS) and Sedimentation Velocity Analytical Ultracentrifugation (SV-AUC). Light scattering studies on Component A yielded an estimated experimental molecule weight of the main peak of 147 kDa, which is in line with the theoretical molecular weight of 152 kDa for the trimer. These results confirmed that the Component A drug substance intermediate existed in a trimeric state as anticipated. In addition, very low levels of aggregates were also detected with estimated molecular weights of 279 kDa and 426 kDa that can be attributed to higher order oligomers of Component A (Fig. 12).

The assembly of the vaccine nanoparticle was characterized by SV-AUC during the initial method assessment phase with research-grade Component A. The predominant species (73%) after assembly of Component A with Component B exhibited a molecular weight of 3.71 MDa, which is in line with the theoretical molecular weight of 4.1 MDa for the fully assembled nanoparticle (Fig. 13).

3.6. Stability of Component A

Previous excipient screening efforts at the IPD identified 50 mM Tris, 150 mM NaCl, 100 mM Arginine, 5% sucrose, pH 8.0 as a promising formulation for storage of Component A at 5 mg/mL, that is also compatible with storage of the assembled nanoparticle immunogen [18]. The long-term stability of the Component A in this formulation was evaluated at the recommended storage condition (RSC) of $-70\text{ }^{\circ}\text{C}$. Additionally, the stability of the Component A at accelerated storage conditions (ASC) of $-30\text{ }^{\circ}\text{C}$, $5\text{ }^{\circ}\text{C}$, and the stressed storage condition (SSC) of $25\text{ }^{\circ}\text{C}$ were also evaluated to support handling and possible excursions. The formulation effectiveness and suitability were verified to minimize degradation that may occur during storage. The attributes and corresponding analytical methods used to assess the stability of the formulation included main peak by SE-UHPLC, nanoparticle assembly capability by SEC, purity by reduced CE-SDS, and potency by the binding assay.

The stability study results showed that Component A remains stable through 12 months of storage at RSC of $-70\text{ }^{\circ}\text{C}$. There were no

significant changes observed up to 12 months for the main peak due to aggregation by SE-UHPLC or purity due to clipping by rCE-SDS. Moreover, Component A remained fully capable of forming the nanoparticle by assembly with Component B and potent with respect to binding to hACE2 receptor.

Component A was found to be chemically and physically stable at ASC of $-30\text{ }^{\circ}\text{C}$ up to 6 months. A slight decrease in main peak by SE-UHPLC and purity by rCE-SDS was observed through 6 months of storage at the ASC of $5\text{ }^{\circ}\text{C}$ and 1 month of storage at the SSC of $25\text{ }^{\circ}\text{C}$. Correspondingly, a decreasing trend in the potency of the Component A was also observed, but not for the capability of forming nanoparticle assembly. The results of those studies are summarized in Fig. 14.

4. Discussion

The rapid development of safe and effective vaccines in response to the SARS-CoV-2 pandemic is a remarkable technological achievement that has saved many lives [19]. Here we have described upstream and downstream PD for the antigen-bearing component of a two-component self-assembling nanoparticle vaccine for SARS-CoV-2. The Phase 1 clinical trial evaluating this vaccine candidate that began in June 2021, as well as that of a closely related vaccine candidate based on the same nanoparticle immunogen which began in February 2021 [4], were the first clinical studies of computationally designed two-component nanoparticle vaccines. The urgency of pandemic response efforts demanded rapid development of this molecule, without well-established process platforms, thus presenting several interesting PD challenges. Here we outline these challenges and the solutions we identified to overcome them.

4.1. Slow pool recovery

Cell line development is often on critical path for MCB creation and enables the generation of representative materials for downstream and analytical method development. Component A cell pools recovered unexpectedly slowly after transfection. To address recovery issues, the PD team evaluated different signal peptides, codon sets, and culture temperatures. It was found that both the original signal peptide (μ phosphatase) and a recovery temperature at $36\text{ }^{\circ}\text{C}$ were favorable for recovery. In contrast, the proprietary signal peptide typically used for mAb-based molecules was not optimal for this molecule. In addition,

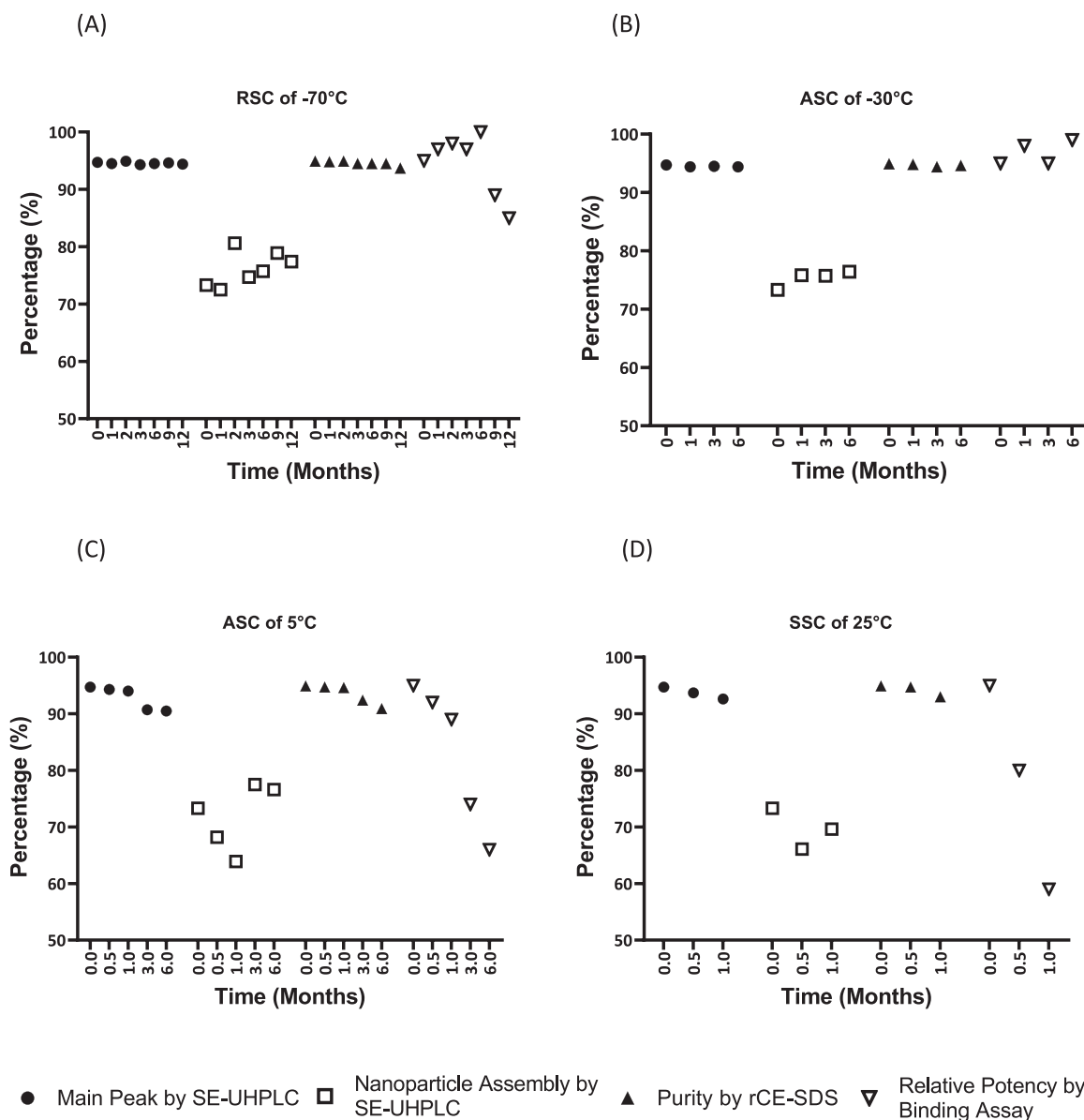


Fig. 14. The stability of Component A at different storage conditions. (A) RSC of -70°C . (B) ASC of -30°C . (C) ASC of 5°C . (D) SSC of 25°C .

reducing the temperature to 32°C also did not lead to pool recovery for this CHO-derived host, unlike what has been reported in the literature [3]. To avoid delays to other activities, the team also decided to use HEK293 transient expression with a normalized harvest titer of 0.05 to supply early development activities at 2 L scale. This approach afforded additional cell line recovery time, and it was understood that HEK293-derived material could be different from that of CHO in terms of composition and product quality profile, specifically with respect to glycans, HMW species, and other impurities. Potential material differences were de-risked in two ways. First, a glycan profiling study was performed to demonstrate that the glycans were functionally non-obligate and uninvolved in nanoparticle assembly, confirming modeling studies. Second, process challenge and spiking studies around the anticipated worst-case product and process-related impurity levels were included in purification development to ensure sufficient process robustness.

4.2. Viral clearance

The expected overall process viral clearance capability was

challenging to estimate due to limited prior knowledge of log reduction of virus (LRV) by unit operation of Component A. Consequently, the team performed a mock viral clearance study ($n = 1$) on the HIC and MMC chromatography unit operations with representative supply material to estimate the LRV of those steps. The RT-qPCR assay was used rather than the traditional but costly median tissue culture infectious dose (TCID_{50}) assay to provide estimated results. Using the prior knowledge for viral inactivation LRV, viral filtration LRV, and retrovirus-like particle (RLP) numbers, it was estimated that at least 15 overall processes LRV would be needed suggesting that a combined 3 LRV would be required between HIC and MMC. The mock study determined that HIC and MMC provided > 4 LRV, providing confidence that the process would meet the overall LRV needed.

4.3. Operational challenges

The team also encountered operational challenges during the NHU toxicology lot production. Pressure accumulation and flow decay was identified during HIC, likely attributable to bed consolidation despite operating within the manufacturer's recommended linear flow velocity

range for the resin. To complete the lot, the existing automation was overridden and manually operated controlling at constant pressure with a variable flow rate. Although this significantly increased the step duration, it was within acceptable pool hold durations, operationally manageable, and enabled successful run completion. To avoid repeating the scenario, new automation was developed for the GMP run, where the HIC operation was controlled at fixed pressure with variable flow rate interlocked with high and high-high alarm thresholds to avoid pressure events that could adversely impact the run.

4.4. Depth filtration redevelopment

Secondly, during the NHU toxicology run, the team observed fouling during depth filtration of neutralized viral inactivated pool despite demonstrating greater than 70 L/m² loading on small scale (23 cm² filter area) using CHO-derived materials. During the NHU lot, filtration of the nVIP required numerous filter changes and only yielded < 20 L/m² loading and a step yield of < 50%. Furthermore, results suggested the process was inherently prone to product loss at approximately 8–10 g/m² and up to 12–15 g/L during harvesting. The product loss was attributed to non-specific filter adsorption that was exacerbated by low throughput. The low productivity of the stable cell pool generated a normalized titer of approximately 0.5, and assuming the previously observed 10 g/m² product loss, would corresponded to 0% and 50% harvest yields, respectively. If the loading level could be increased to 100 L/m², then the harvest yield could be dramatically improved to 80%. The depth filtration steps were redeveloped with the aim of avoiding filter fouling and product loss by increasing throughput (> 100 L/m²). Due to time constraints and filter constraints, pool treatment options were not further studied due to increased study complexity. Yields and throughput were significantly improved with depth filtration redevelopment.

5. Conclusion

In conclusion, the cell line, upstream, downstream, analytical and formulation PD efforts we developed enabled the rapid entry of a new vaccine modality—computationally designed protein nanoparticles—into the clinic. Given that two other computationally designed two-component nanoparticle vaccines (for RSV and influenza) are also in Phase 1 clinical trials (one of which uses I53–50 as a scaffold), future efforts to develop platform methods that could be used across component A molecules displaying different antigens could be broadly useful for facilitating clinical development of nanoparticle vaccines for many different indications.

Data availability

The data that has been used is confidential.

Acknowledgements

The authors would like to thank the IPD Core Laboratories, A.C. Walls, and D. Veessler for the initial discovery and evaluation of the nanoparticle vaccine candidate. The authors would also like to thank the Amgen Rapid Analytics group, Pilot Plant Operations, Clinical Manufacturing team, Viral Clearance group, Justin Bown, Leandro Fernandez, Charilyn Tejamo, Teresa Barrier, Nancy Jiao, Ronandro De Guzman, Lynn Long, Agatha Bishnoi, Jeanne Go and Process Development leadership for their support with this project. This work was supported by Amgen, the Bill & Melinda Gates Foundation (OPP1156262), and the Audacious Project at the Institute for Protein Design.

Appendix A. Supporting information

Supplementary data associated with this article can be found in the

online version at doi:10.1016/j.procbio.2023.03.014.

References

- [1] B. Kelley, Developing therapeutic monoclonal antibodies at pandemic pace, *Nat. Biotechnol.* 38 (5) (2020) 540–545.
- [2] B. Kelley, T. Renshaw, M. Kamarck, Process and operations strategies to enable global access to antibody therapies 37 (3) (2021), e3139.
- [3] A.C. Walls, B. Fiala, A. Schäfer, S. Wrenn, M.N. Pham, M. Murphy, L.V. Tse, L. Shehata, M.A. O'Connor, C. Chen, M.J. Navarro, M.C. Miranda, D. Pettie, R. Ravichandran, J.C. Kraft, C. Ogohara, A. Palser, S. Chalk, E.C. Lee, K. Guerriero, E. Kepl, C.M. Chow, C. Sydeman, E.A. Hodge, B. Brown, J.T. Fuller, K. H. Dinnon 3rd, L.E. Gralinski, S.R. Leist, K.L. Gully, T.B. Lewis, M. Guttman, H. Y. Chu, K.K. Lee, D.H. Fuller, R.S. Baric, P. Kellam, L. Carter, M. Pepper, T. P. Sheehan, D. Veessler, N.P. King, Elicitation of Potent Neutralizing Antibody Responses by Designed Protein Nanoparticle Vaccines for SARS-CoV-2, *Cell* 183 (5) (2020) 1367–1382, e17.
- [4] J.Y. Song, W.S. Choi, J.Y. Heo, J.S. Lee, D.S. Jung, S.-W. Kim, K.-H. Park, J.S. Eom, S.J. Jeong, J. Lee, K.T. Kwon, H.J. Choi, J.W. Sohn, Y.K. Kim, J.Y. Noh, W.J. Kim, F. Roman, M.A. Ceregado, F. Solmi, A. Philippot, L. Carter, D. Veessler, N. King, H. Kim, J.H. Ryu, S.J. Lee, Y.W. Park, H.K. Park, H.J. Cheong, Safety and immunogenicity of a SARS-CoV-2 recombinant protein nanoparticle vaccine (GBP510) adjuvanted with AS03: a phase 1/2, randomized, placebo-controlled, observer-blinded trial, 2022: 2022.03.30.22273143.
- [5] J.B. Bale, S. Gonen, Y. Liu, W. Sheffler, D. Ellis, C. Thomas, D. Cascio, T.O. Yeates, T. Gonen, N.P. King, D. Baker, Accurate design of megadalton-scale two-component icosahedral protein complexes, *Sci. (N. Y., N. Y.)* 353 (6297) (2016) 389–394.
- [6] S.W. Fullerton, J.S. Griffiths, A.B. Merkel, M. Cheriyan, N.J. Wymer, M.J. Hutchins, C.A. Fierke, E.J. Toone, J.H. Naismith, Mechanism of the Class I KDPG aldolase, *Bioorg. Med. Chem.* 14 (9) (2006) 3002–3010.
- [7] S. Klinke, V. Zylberman, H.R. Bonomi, I. Haase, B.G. Guimarães, B.C. Braden, A. Bacher, M. Fischer, F.A. Goldbaum, Structural and kinetic properties of lumazine synthase isoenzymes in the order Rhizobiales, *J. Mol. Biol.* 373 (3) (2007) 664–680.
- [8] A.J. Wargacki, T.P. Wörner, M. van de Waterbeemd, D. Ellis, A.J.R. Heck, N. P. King, Complete and cooperative in vitro assembly of computationally designed self-assembling protein nanomaterials, *Nat. Commun.* 12 (1) (2021) 883.
- [9] J. Marcandalli, B. Fiala, S. Ols, M. Perotti, W. de van der Schueren, J. Snijder, E. Hodge, M. Benhaim, R. Ravichandran, L. Carter, W. Sheffler, L. Brunner, M. Lawrenz, P. Dubois, A. Lanzavecchia, F. Sallusto, K.K. Lee, D. Veessler, C. E. Correnti, L.J. Stewart, D. Baker, K. Loré, L. Perez, N.P. King, Induction of potent neutralizing antibody responses by a designed protein nanoparticle vaccine for respiratory syncytial virus, *Cell* 176 (6) (2019) 1420–1431, e17.
- [10] S. Boyoglu-Barnum, D. Ellis, R.A. Gillespie, G.B. Hutchinson, Y.J. Park, S.M. Moin, O.J. Acton, R. Ravichandran, M. Murphy, D. Pettie, N. Matheson, L. Carter, A. Creanga, M.J. Watson, S. Kephart, S. Ataca, J.R. Vaile, G. Ueda, M.C. Crank, L. Stewart, K.K. Lee, M. Guttman, D. Baker, J.R. Mascola, D. Veessler, B.S. Graham, N.P. King, M. Kanekiyo, Quadrivalent influenza nanoparticle vaccines induce broad protection, *Nature* 592 (7855) (2021) 623–628.
- [11] MilliporeSigma, Millistak+® Pod Dispos. depth Filter Syst. (2019) 1–8.
- [12] Z. Zhang, Large-scale identification and quantification of covalent modifications in therapeutic proteins, *Anal. Chem.* 81 (20) (2009) 8354–8364.
- [13] Z. Zhang, Retention time alignment of LC/MS data by a divide-and-conquer algorithm, *J. Am. Soc. Mass Spectrom.* 23 (4) (2012) 764–772.
- [14] Z. Zhang, B. Shah, Prediction of collision-induced dissociation spectra of common N-glycopeptides for glycoform identification, *Anal. Chem.* 82 (24) (2010) 10194–10202.
- [15] B. Shah, X.G. Jiang, L. Chen, Z. Zhang, LC-MS/MS peptide mapping with automated data processing for routine profiling of N-glycans in immunoglobulins, *J. Am. Soc. Mass Spectrom.* 25 (6) (2014) 999–1011.
- [16] H. Zhao, P.H. Brown, P. Schuck, On the distribution of protein refractive index increments, *Biophys. J.* 100 (9) (2011) 2309–2317.
- [17] Y. Watanabe, J.D. Allen, D. Wrapp, J.S. McLellan, M. Crispin, Site-specific glycan analysis of the SARS-CoV-2 spike, *Sci. (N. Y., N. Y.)* 369 (6501) (2020) 330–333.
- [18] P.S. Arunachalam, A.C. Walls, N. Golden, C. Atyeo, S. Fischinger, C. Li, P. Aye, M. J. Navarro, L. Lai, V.V. Edara, K. Röltgen, K. Rogers, L. Shirreff, D.E. Ferrell, S. Wrenn, D. Pettie, J.C. Kraft, M.C. Miranda, E. Kepl, C. Sydeman, N. Brunette, M. Murphy, B. Fiala, L. Carter, A.G. White, M. Trisal, C.L. Hsieh, K. Russell-Lodrigue, C. Monjure, J. Dufour, S. Spencer, L. Doyle-Meyers, R.P. Bohm, N. J. Maness, C. Roy, J.A. Plante, K.S. Plante, A. Zhu, M.J. Gorman, S. Shin, X. Shen, J. Fontenot, S. Gupta, D.T. O'Hagan, R. Van Der Most, R. Rappuoli, R.L. Coffman, D. Novack, J.S. McLellan, S. Subramaniam, D. Montefiori, S.D. Boyd, J.L. Flynn, G. Alter, F. Villinger, H. Kleanthous, J. Rappaport, M.S. Suthar, N.P. King, D. Veessler, B. Pulendran, Adjuvanting a subunit COVID-19 vaccine to induce protective immunity, *Nature* 594 (7862) (2021) 253–258.
- [19] S. Mallapaty, E. Callaway, M. Kozlov, H. Ledford, J. Pickrell, R. Van Noorden, How COVID vaccines shaped 2021 in eight powerful charts, *Nature* 600 (7890) (2021) 580–583.